AN ATOMISTIC-TO-MACROSCOPIC WORKFLOW FOR GAS–SURFACE INTERACTION MODELING IN VLEO WITH A ROUTE TOWARD EXPERIMENTAL VALIDATION

J. Boskovic*, M. Schütte†, N. Segreto‡, L. K. H. Kruse‡, A. Riffelt‡, K.-S. Ellenberger†, A. Schlitzer†, L. Voigt†, S. Hocker§, H. Lipp§, J. Roth§, J. Kästner‡, S. Löhle†, A. Beck*, M. Pfeiffer†, S. Fasoulas†

* Institute of Aerodynamics and Gas Dynamics, University of Stuttgart, Stuttgart, Germany
† Institute of Space Systems, University of Stuttgart, Stuttgart, Germany
‡ Institute for Theoretical Chemistry, University of Stuttgart, Stuttgart, Germany
§ Institute for Functional Matter and Quantum Technologies, University of Stuttgart, Stuttgart, Germany

Abstract

Predicting aerodynamic forces in very low Earth orbit (VLEO) requires a gas–surface interaction model that connects atomic-scale surface mechanisms to spacecraft-scale quantities. This paper presents the common numerical and experimental workflow of projects A01–A04 within CRC 1667 ATLAS. At the atomistic scale, density-functional calculations, machine-learned interatomic potentials, classical force fields, and molecular dynamics simulations are used to resolve hyperthermal atomic-oxygen impacts on representative oxide surfaces. The resulting conditional statistics of reflection, adsorption, desorption, energy transfer, and momentum transfer provide the input for a data-driven scattering kernel. At the mesoscopic scale, a conditional variational autoencoder samples reflected particle states as a wall boundary condition in Direct Simulation Monte Carlo (DSMC). Surface momentum fluxes are then integrated into lift and drag coefficients, forces, and moments. Multi-fidelity Monte Carlo combines a limited number of high-fidelity kinetic simulations with inexpensive panel-method evaluations to propagate environmental uncertainty at tractable cost. A complementary validation route is being established using a ground-based atomic-oxygen facility, its numerical reconstruction, and diagnostics for particle flux, number density, velocity, and composition. The main contribution of this paper is the explicit definition of the quantities transferred between scales, the present maturity of each interface, and a two-level validation strategy that first establishes the incident facility flow and subsequently assesses the surface-response model. The workflow provides a consistent route from individual oxygen impacts to mission-relevant aerodynamic predictions without hiding unresolved model-form and measurement uncertainties at the scale interfaces.

Keywords

very low Earth orbit; gas–surface interaction; atomic oxygen; molecular dynamics; Direct Simulation Monte Carlo; scattering kernel; uncertainty quantification; experimental validation

1. INTRODUCTION

Spacecraft operating in very low Earth orbit (VLEO) encounter a rarefied, compositionally variable, and strongly non-equilibrium environment. Atomic oxygen is a major contributor to the incident particle flux and combines hyperthermal impact energies with high chemical reactivity. The resulting gas-surface interaction (GSI) governs the momentum and energy transferred to exposed surfaces, and therefore contributes directly to aerodynamic drag, lift, torques, thermal loads, and material evolution. Reliable prediction of these quantities is relevant to lifetime assessment, attitude and orbit control, geometry optimization, and atmosphere-breathing propulsion concepts.

Common engineering wall models represent reflection through a small number of accommodation parameters or through a mixture of idealized specular and diffuse processes. Such models are computationally efficient, but they cannot generally resolve the simultaneous dependence on incident velocity, incidence angle, material, atomic-scale roughness, surface coverage, temperature, and chemical reaction pathway. Atomistic simulations provide access to this missing mechanism-level information. They are, however, too expensive to be applied at the length and time scales of a complete rarefied-flow problem. A usable workflow must therefore transfer a statistically complete but computationally compact surface model from the atomistic to the mesoscopic scale.

Recent work within ATLAS demonstrated two central parts of this transfer. Molecular-dynamics simulations revealed the dependence of atomic-oxygen reflection and adsorption on alumina surface structure and incidence conditions [1]. A conditional generative model was subsequently trained on molecular-dynamics scattering data and embedded as a wall kernel for aerodynamic calculations [2]. In parallel, a multi-fidelity

CC BY 4.0

doi: 10.25967/680070

framework was developed to propagate atmospheric and attitude uncertainty through high-fidelity direct simulation Monte Carlo (DSMC) at reduced computational cost [3]. These developments establish important numerical links, but a predictive chain also requires an experimentally characterized reference environment and a validation strategy that distinguishes uncertainty in the incident flow from uncertainty in the surface response.
This paper consolidates the numerical and experimental activities of ATLAS projects A01–A04 into one interface-centered workflow. Its contributions are:

1) a common mathematical description of the information transferred from atomistic trajectories to a mesoscopic scattering kernel and then to macroscopic aerodynamic quantities;
2) a status-based synthesis of the demonstrated A01/A02 links and the developing A03/A04 facility and diagnostic capabilities; and
3) a two-level route for calibration and validation that separates characterization of the facility flow from assessment of the GSI response.

The paper deliberately distinguishes results already demonstrated in published or completed studies from capabilities that are in progress or planned.

2. CROSS-SCALE FRAMEWORK AND INTERFACE QUANTITIES

Figure 1 summarizes the workflow. A01 resolves individual impact mechanisms and produces ensembles of trajectories. A02 first compresses these ensembles into a probabilistic wall kernel and then propagates wall events through DSMC to aerodynamic coefficients and uncertainty estimates. A03 and A04 establish the facility flow and its diagnostics. They form a validation loop rather than an additional scale appended to the numerical chain.
An incident particle state is denoted by

$$\boldsymbol{x}_i = (\boldsymbol{v}_i, s_i, T_s, \mathcal{S}), \tag{1}$$

where $\boldsymbol{v}_i$ and s_i are the incident velocity and species, T_s is the surface temperature, and $\mathcal{S}$ summarizes the material and surface state. Depending on the model maturity, $\mathcal{S}$ may include crystallographic or amorphous structure, roughness, oxygen coverage, and other descriptors of chemical state. The atomistic simulation returns an outcome

$$\boldsymbol{y} = (r, \boldsymbol{v}_r, s_r, \Delta E_s), \tag{2}$$

where r labels the event class, for example reflection, adsorption, or desorption; $\boldsymbol{v}_r$ and s_r describe the outgoing particle or fragment; and ΔE_s is the energy transferred to or stored in the surface. An ensemble of impacts defines the conditional kernel

$$\mathcal{K}(\boldsymbol{y} \mid \boldsymbol{x}_i) = p(r, \boldsymbol{v}_r, s_r, \Delta E_s \mid \boldsymbol{v}_i, s_i, T_s, \mathcal{S}). \tag{3}$$

This expression makes the intended interface explicit. A scalar accommodation coefficient is a projection of eq. (3); it is not, in general, a sufficient representation of the joint angular, velocity, species, and reaction statistics.
At the mesoscopic scale, repeated draws from $\mathcal{K}$ provide post-collision states for particles striking a wall. The time-averaged force follows from the net momentum flux,

$$\boldsymbol{F} = \frac{1}{\Delta t} \sum_{k \in \mathcal{C}(\Delta t)} w_k m_k \left(\boldsymbol{v}_{i,k} - \boldsymbol{v}_{r,k} \right), \tag{4}$$

where $\mathcal{C}(\Delta t)$ is the set of wall events during the sampling interval, and w_k and m_k are the particle weight and molecular mass. Surface integration and normalization yield C_D, C_L, and corresponding moment coefficients. The crucial point is that changes in atomistic scattering statistics can be propagated without reducing them a priori to one global wall parameter.

3. ATOMISTIC GAS–SURFACE INTERACTION CHARACTERIZATION

3.1. Hierarchy of Atomistic Models

A01 combines complementary atomistic descriptions. Density-functional calculations provide chemically accurate energies and forces for representative configurations and reaction paths. Properties obtained at this level, such as adsorption energies and surface reactivity, are used to identify suitable surface materials. Machine-learned interatomic potentials approximate this reference information at substantially larger sample counts. These potentials enable statistical impact studies, including analyses of surface composition under VLEO conditions, energetic behavior under repeated impacts, and particle scattering. Classical polarizable force fields permit still larger or more structurally complex systems, including amorphous and rough surfaces, at the cost of a more restricted description of chemical reactivity.
The production calculation consists of a prepared surface, a specified temperature, and repeated AO impacts with prescribed or sampled incident velocities. Each trajectory is classified by its long-time outcome, and we record reflected velocity, energy transfer, adsorption, and possible product desorption. The hierarchy is not intended to make all atomistic models interchangeable. Instead, overlapping cases determine which observables can be transferred reliably from each fidelity level.

3.2. Scattering, Roughness, and Surface Chemistry

Published alumina calculations show that the angular and speed distributions of reflected oxygen depend strongly on incidence angle and surface morphology [1]. Smooth surfaces and grazing incidence promote a more focused, quasi-specular response, whereas atomic- and nanometer-scale roughness broaden the distribution and increase energy transfer. Lower incident velocities strengthen the influence of attractive surface sites and can increase adsorption or selectively allow only faster particles to escape. These observations explain

CC BY 4.0

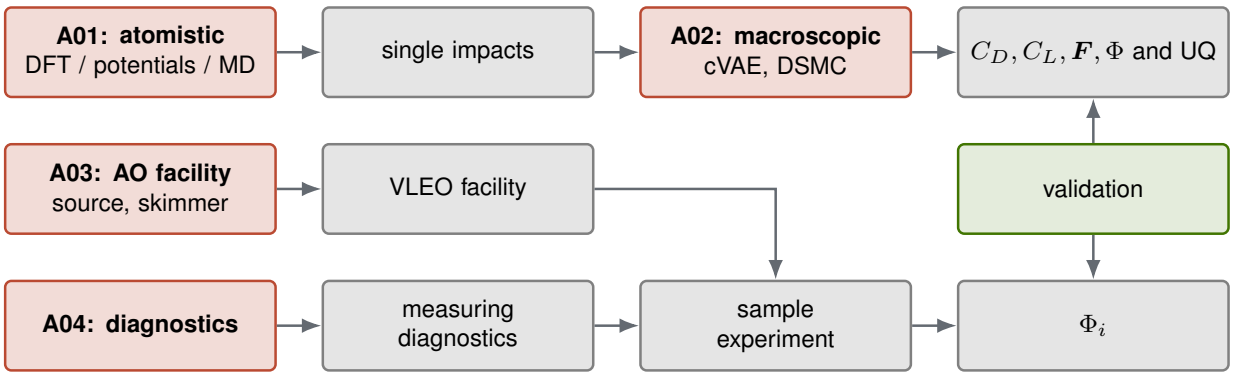


FIG 1. Information flow across ATLAS projects A01–A04. The upper branch transfers atomistic trajectory information to a probabilistic wall kernel, mesoscopic rarefied-flow simulation, and macroscopic aerodynamic quantities. The lower branch provides the experimentally characterized boundary condition.

TAB 1. Maturity of the principal interfaces in the proposed workflow.

Interface	Transferred quantity	Present evidence and limitation	Status
A01 → A02	Conditional reflected-velocity distributions for selected incident states and alumina surfaces	Demonstrated using molecular-dynamics data and a cVAE kernel [2]; the productive kernel does not yet represent every surface-reaction and evolving-coverage pathway in eq. (3).	demonstrated / partial
A02 meso → macro	Momentum fluxes, C_D, C_L, forces, and moments	Demonstrated for canonical aerodynamic cases; differences from Maxwell-type baselines show sensitivity to the wall model.	demonstrated
A02 → UQ	Shared high-/low-fidelity samples and moment estimators	MFMC is verified and benchmarked for DSMC and panel models [3]; performance depends on moment correlation and cost ratio.	demonstrated
A03 ↔ A04	Local facility flow, measurement calibration, and uncertainty	Facility reconstruction, skimmer studies, and diagnostic development are ongoing; velocity and low-density measurement ranges remain active constraints.	in progress
Experiment → GSI validation	Incident distribution and independent surface-response observable	Validation logic is defined in section 6; a complete end-to-end data set has not yet been acquired.	planned

why a fixed specular–diffuse mixing coefficient is not transferable across incident conditions.

The chemical description also changes the inferred outcome probabilities. Machine-learned potentials fitted to electronic-structure data predict substantially stronger adsorption on the investigated crystalline alumina surface than the classical force field. At the same time, the reflected angular trends remain qualitatively consistent [1].

Current sequential-impact calculations extend the isolated-impact picture toward an oxygen-covered surface. At a surface temperature of $300\,\mathrm{K}$ and an impact velocity near $8\,\mathrm{km\,s^{-1}}$, the simulated alumina surface approaches a statistically stationary coverage distribution, showing the importance of reactive simulations. A fraction of the incident AO recombines with adsorbed oxygen to form O_2, desorbing with a different energy distribution than atomic oxygen. This reflects a distinct, reactivity-driven energy-transfer channel. Since the exothermic bond-formation energy is partly channeled into the fragment's motion rather than into the surface, the desorbing O_2 carries away more energy than atomic oxygen. Furthermore, peroxide formation, molecular-oxygen formation, and desorption produce energy partitions that an assumption of complete thermal equilibration before desorption does not capture. Thus, besides roughness, surface morphology, and incident conditions, surface chemical reactivity is a fourth factor that influences particle scattering. These are ongoing A01 results and are therefore used here to define the future kernel state space rather than being claimed as fully propagated A02 wall chemistry.

3.3. Required Output for the Next Scale

For the A01–A02 transfer, trajectory data must be stored together with the complete conditioning variables, not only the outgoing velocity. At minimum, the database requires the incident velocity vector, surface temperature, material identifier, surface-state identifier, event label,

CC BY 4.0

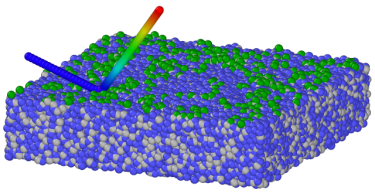


FIG 2. Representative molecular-dynamics impact trajectories on an amorphous alumina surface. Ensembles of trajectories provide conditional angular and velocity distributions and distinguish reflected, adsorbed, and reactive outcomes.

reflected or product velocity, and energy/momentum balance. Finite-ensemble uncertainty and the fidelity of the interatomic model must remain attached to the data. An immediate development priority is to define a compact descriptor of the evolving surface state $\mathcal{S}$ that is both meaningful to the atomistic model and usable as a condition in the mesoscopic kernel. To make the kernel accessible, the database must include coverage-dependent desorption probabilities. The surface-state descriptor should distinguish between clean, partially covered, and fully covered surfaces, as well as different types of adsorbed species. This will allow for accurate modeling of the gas-surface interactions in the mesoscopic simulations.

4. ATOMISTIC-TO-MESOSCOPIC TRANSFER

Atomistic simulations provide highly resolved insights into the GSI, enabling a detailed characterization of microscopic scattering processes. However, to evaluate the aerodynamic drag of an entire satellite, mesoscale methods such as DSMC are required. In DSMC, particle scattering at the surface is modeled through so-called scattering kernels $\mathcal{K}(\boldsymbol{v}_\mathrm{r}|\boldsymbol{v}_\mathrm{i})$, which represent conditional probability density functions. Traditional scattering kernels rely on predefined assumptions about the scattering behavior and incorporate accommodation coefficients. These coefficients are difficult to determine experimentally and are often poorly known. To obtain a more physically detailed scattering model, atomistic simulations can be used to derive the reflected-velocity distributions for specific incident velocities. To integrate these data-driven kernels into DSMC and to generalize beyond the discrete incident velocities sampled in atomistic simulations, A02 uses machine-learning (ML) models such as conditional variational autoencoder (cVAE) or conditional normalizing flow (cNF) [2, 4]. These models learn the conditional distribution of reflected velocities from A01 molecular dynamics (MD) data and can subsequently be used as scattering kernels within DSMC frameworks such as the open-source code PICLas [5].

Both models transform a normally distributed latent variable $\boldsymbol{z} \sim \mathcal{N}(\mathbf{0}, \boldsymbol{I})$ into the complex reflected-velocity distribution conditioned on the incident velocity $\boldsymbol{v}_\mathrm{i}$. In the cVAE, this transformation is performed by a single decoder network, whereas the cNF uses a sequence of coupling layers, each equipped with its own neural network. The predicted reflected velocity is thus given by

$$\boldsymbol{v}_{\mathrm{r,p}} = g_\theta(\boldsymbol{z}, \boldsymbol{v}_\mathrm{i}), \qquad \boldsymbol{z} \sim \mathcal{N}(\mathbf{0}, \boldsymbol{I}), \tag{5}$$

where g_θ denotes either the cVAE decoder or the series of coupling layers in the cNF. In the case of the cNF, physical constraints such as the detailed-balance relation can even be incorporated directly into the training process. Both models are evaluated on unseen data, including incident velocities outside the training range. While the cNF attains higher accuracy than the cVAE, the cVAE enables significantly faster data generation.

For amorphous alumina, the ML models are trained on MD data obtained using classical interatomic potentials. The resulting scattering models are subsequently integrated into the DSMC method in PICLas. Aerodynamic coefficients (lift C_L and drag C_D) are computed under VLEO conditions for a range of angles of attack α.

The overall workflow, from atomistic simulation through ML-based scattering kernels to the derivation of aerodynamic coefficients, is illustrated in Figure 3. The resulting coefficients are shown in Figure 4, where the ML-based models are compared against a classical Maxwell model that represents GSIs as a superposition of diffuse and specular reflection. The relative contribution of each reflection type is governed by the accommodation coefficient σ. For selected angles of attack, aerodynamic coefficients directly derived from MD data are also included.

The comparison reveals that the simple Maxwell model cannot reproduce the correct aerodynamic behavior across the investigated conditions. In contrast, both ML models show excellent agreement with the MD-derived coefficients. At low angles of attack, the scattering behavior is closer to predominantly specular reflection, whereas at high angles of attack it approaches diffuse reflection.

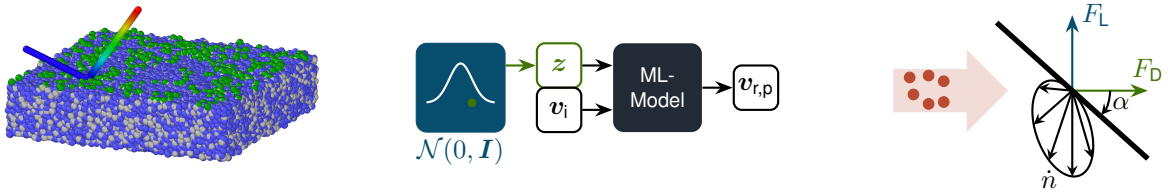
The aerodynamic coefficients obtained from the ML-based scattering kernels can be readily used in panel methods such as ADBSat [6], enabling fast yet physically accurate aerodynamic evaluations of satellite geometries. Recent work has already applied ML-derived aerodynamic coefficients to investigate orbit-control strategies that exploit aerodynamic forces in VLEO [7]. This demonstrates the practical relevance of high-fidelity scattering models for attitude and orbit control in the emerging regime of VLEO.

5. MESOSCOPIC-TO-MACROSCOPIC PROPAGATION AND UQ

5.1. Rarefied-Flow Force Prediction

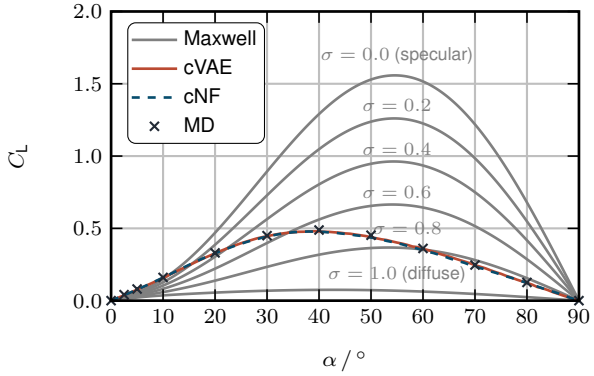
The DSMC method represents the gas by weighted simulation particles and separates particle motion, collisions, and wall interactions over a time step [8]. PICLas provides the high-fidelity particle framework used here [9]. For every surface collision, the incident particle state is supplied to the wall model, and the reflected

CC BY 4.0

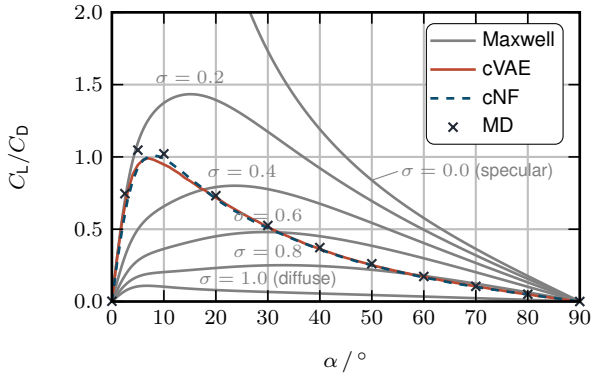


(a) Atomistic trajectories and outcome data. (b) Conditional sampling of reflected velocity. (c) DSMC propagation to lift and drag.

FIG 3. Demonstrated numerical transfer from A01 molecular-dynamics data through a ML wall kernel to A02 rarefied-flow force prediction.



(a) Lift coefficient



(b) Lift-to-drag ratio

FIG 4. Aerodynamic coefficients for a flat plate in VLEO conditions derived by DSMC simulation with the cVAE, cNF, and Maxwell scattering model [4].

state is sampled from $\mathcal{K}_\theta$. Equation (4) is accumulated by surface element to obtain total forces and moments. For a flat plate, the atomistic/cVAE wall model produces lift and lift-to-drag trends that cannot be reproduced over the full angle range by one constant Maxwell parameter [2]. The discrepancy is a direct measure of wall-model form sensitivity. At spacecraft scale, the same mechanism couples to geometry, shadowing, multiple reflections in concavities, composition, and the local flow regime. Consequently, both the high-fidelity solver and the wall-kernel domain must be specified when an aerodynamic coefficient is reported.

5.2. Multi-Fidelity Uncertainty Propagation

Large Monte Carlo ensembles of PICLas simulations are often prohibitively expensive. A02 therefore combines high-fidelity PICLas/DSMC outputs Q_0 with inexpensive ADBSat panel-model outputs Q_1 [6] evaluated for shared uncertain inputs. For a single low-fidelity control variate, the mean estimator can be written as

$$\widehat{\mu}_{\mathrm{MF}} = \overline{Q}_0^{(n_0)} + \beta \left(\overline{Q}_1^{(n_1)} - \overline{Q}_1^{(n_0)} \right), \qquad n_1 \geq n_0, \tag{6}$$

where the first n_0 samples are shared and β, n_0, and n_1 are chosen from pilot estimates of correlation, variance, and cost. The same construction is applied separately to C_D and C_D^2, after which

$$\mathrm{Var}(C_D) = \mathbb{E}[C_D^2] - \mathbb{E}[C_D]^2 \tag{7}$$

is formed.

The benchmark covers ten Cube, SOAR, scaled GOCE-like, and scaled CHAMP-like cases with uncertain atmosphere, attitude, and surface state [3]. At equal DSMC-equivalent production cost, MFMC reduces the relative root-mean-square error (relRMSE) of both raw drag moments in every case, with case-level median gains from 1.97 to 12.67. For a two-standard-deviation drag-coefficient allowance, the median production gain is 2.99, corresponding under standard Monte Carlo scaling to about 8.9 times the DSMC-only production budget for comparable precision. Including the one-off pilot cost reduces the raw-moment gains to 0.55–4.07, showing that pilot sampling is most beneficial when it can be amortized across a sufficiently large campaign or reused for related studies.

The scaled GOCE-like case at $244\,\mathrm{km}$ illustrates the favorable regime in fig. 5. Its median production relRMSE is reduced by a factor of 4.54 for both $\mathbb{E}[C_D]$ and $\mathbb{E}[C_D^2]$, while the reconstructed drag-variance error is reduced by a factor of 2.54. MFMC approaches the finite-reference Monte Carlo floor for the two directly estimated raw moments as the production budget increases. The variance curve is less monotonic because $\mathrm{Var}(C_D)$ is obtained from the difference of two similar estimates; its accuracy therefore also depends on cancellation and on the covariance of the two moment errors.

The present MFMC results propagate environmental and numerical-model uncertainty. A future end-to-end study must add uncertainty in the learned kernel, the atomistic potential, and the experimentally reconstructed incident distribution without double counting shared sources.

CC BY 4.0

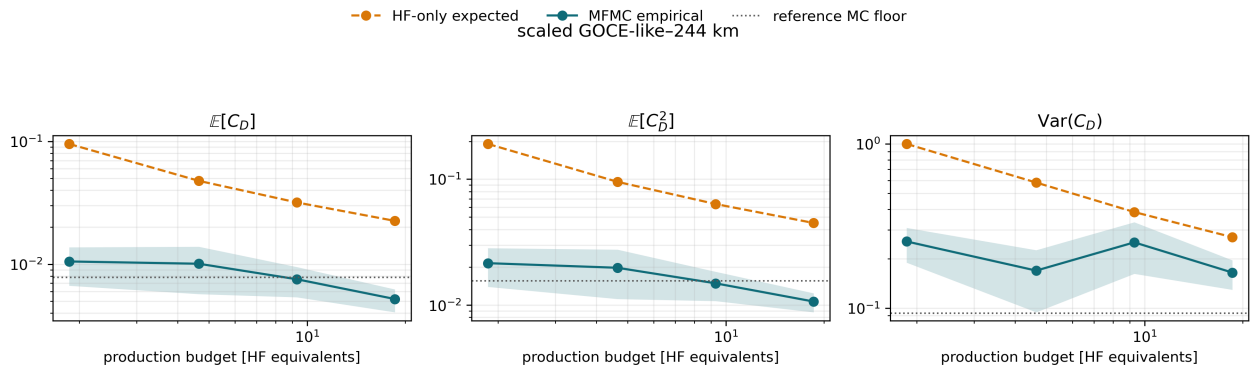


FIG 5. Relative RMSE for the scaled GOCE-like case at $244\,\mathrm{km}$ as a function of DSMC-equivalent production budget. MFMC is compared with the expected high-fidelity-only Monte Carlo error for the mean drag coefficient, second raw moment, and reconstructed variance; shaded bands indicate the empirical MFMC spread and dotted lines the finite-reference Monte Carlo floor [3].

6. EXPERIMENTAL ROUTE TO CALIBRATION AND VALIDATION

6.1. A03: Atomic-Oxygen Facility and Numerical Simulation

A03 is establishing a combined experimental–numerical methodology for ground-based GSI investigation under VLEO-relevant conditions. There are many different approaches to the setup of ground-based AO facilities, each with their own characteristics and operational envelopes [10]. The new AO facility currently under construction features a rather unique design consisting of an inductive plasma generator which produces and thermally expands an oxygen plasma into a pre-vacuum chamber with a background pressure of around 1 Pa. A skimmer serves as the boundary between the pre- and high-vacuum chamber, separating a small AO beam from the oxygen plasma flow inside the pre-chamber. This AO beam will be utilized inside the high-vacuum chamber to perform GSI and material erosion experiments.

In order to design this VLEO facility, a combined approach of experimental characterization and numerical simulation is necessary. The oxygen plasma flow will be characterized with the use of plasma diagnostics for flow velocity, flux density, heat flux, and stagnation pressure. These experimental values will then serve as input boundary conditions for the numerical simulations in the open-source plasma kinetic code PICLas [5, 9]. The results of the numerical simulations will enable the optimal design of the skimmer and vacuum vessels as well as the prediction of the AO beam conditions relevant for the experiments. Figure 6 shows the setup of the numerical simulations and defines the parameters used below. In a preliminary simulation study of the skimmer with estimated oxygen plasma parameters at the nozzle throat of $p_{\mathrm{source}} = 1439\,\mathrm{Pa}$, $T_{\mathrm{source}} = 10\,991\,\mathrm{K}$, and $u_{\mathrm{source}} = 2985\,\mathrm{m\,s^{-1}}$, the influence of the position and shape of the skimmer has been investigated [11].

Due to the large particle density gradients from the exit of the plasma generator to the high vacuum of the material sample chamber, a species-specific particle weighting scheme has been developed in order to improve the efficiency of the numerical simulations over the wide particle density range present inside the facility. The simulation uses a weighting factor of $w_{\mathrm{source}} = 2.5 \times 10^8$ for the estimated source inflow. The background gas is defined by $p_{\mathrm{bg}} = 0.5\,\mathrm{Pa}$, $T_{\mathrm{bg}} = 500\,\mathrm{K}$, and $u_{\mathrm{bg}} = 0\,\mathrm{m\,s^{-1}}$, with a weighting factor of $w_{\mathrm{bg}} = 2.5 \times 10^{10}$. The resulting total stream velocity is shown in Figure 7. A skimmer position x_{pos} of $380\,\mathrm{mm}$, diameter d of $1\,\mathrm{mm}$, and length l of $5\,\mathrm{mm}$ yield a predicted particle flux $\dot{n}$ near $7.8\times10^{18}\,\mathrm{m^{-2}\,s^{-1}}$ and a stream velocity above $6\,\mathrm{km\,s^{-1}}$. The resulting particle flux at the sample position is in a VLEO-relevant range, while the velocity remains below the desired representative condition. The result is highly sensitive to the assumed source inflow and will therefore change when newly measured parameters are used.

The final numerical results will be validated against measurements of the AO beam obtained using a mass spectrometer and other diagnostics developed by project A04 in the high-vacuum chamber, as detailed in the following section.

6.2. A04: Diagnostic Coverage and Traceability

The main objective of project A04 is the diagnostic characterization of atomic oxygen, the main constituent of the VLEO atmosphere. This leads to two main requirements: first, the development and application of diagnostic methods for atomic oxygen in the facility developed by project A03; and second, in situ measurements of the atmosphere at relevant VLEO altitudes. The amperometric solid-state electrolyte sensor FIPEX [12] is the primary measurement method and links the two applications because it can be used both in ground tests and on a future satellite. This ultimately enables a direct comparison between in situ atmospheric measurements and the conditions generated in the ground-based test facility.

Extending the FIPEX measurement range toward the low number densities relevant to VLEO requires a new sensor design with an increased active area. The larger sensor area is expected to enhance the signal at low number densities, requiring corresponding adaptations of the heater and electrode geometries to ensure suitable thermal and electrochemical operating conditions. For the characterization of the ground-based ATOX facil-

CC BY 4.0

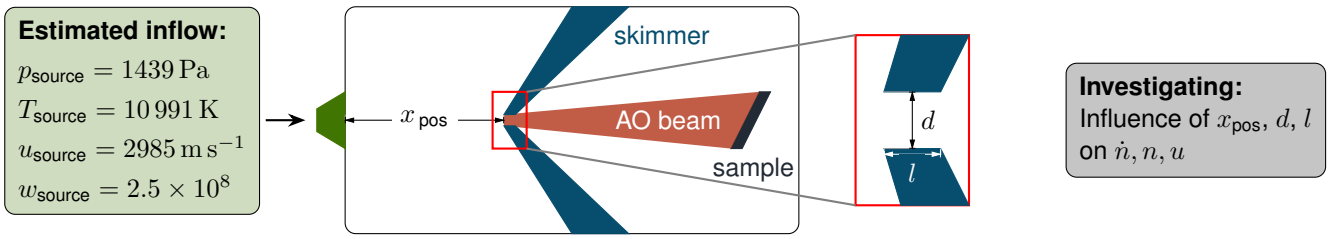


FIG 6. Setup of numerical simulations for a study of the skimmer with estimated inflow conditions.

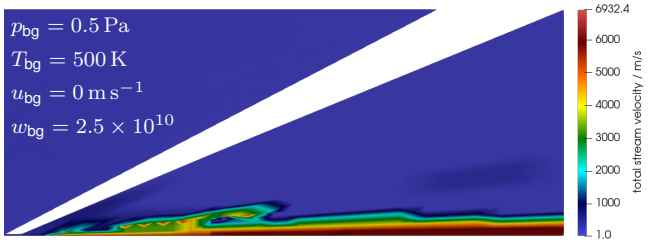


FIG 7. Total stream velocity from a rotationally symmetric simulation with variable particle weighting.

ity, complementary optical and laser-based diagnostics, including TALIF [13], VUV spectroscopy [14], and THz absorption spectroscopy [15], are being investigated for conditions in which sufficient optical depth or excitation signal is available. These spectroscopic techniques are restricted to ground-based diagnostics and are not intended for in situ measurements in VLEO. Since no single diagnostic technique covers the complete operating envelope, the validation boundary conditions are established by combining overlapping diagnostic methods and accounting for their respective calibration uncertainties.

Taken together, A03 and A04 do not yet provide a final, experimentally validated operating envelope. The skimmer case considered here defines a preliminary numerical design point based on estimated source and background conditions. It predicts a particle flux near $7.8 \times 10^{18}\,\mathrm{m^{-2}\,s^{-1}}$ and a stream velocity above $6\,\mathrm{km\,s^{-1}}$ at the sample location. While the predicted flux lies in a VLEO-relevant range, the velocity remains below the desired representative condition and both quantities are sensitive to the assumed source inflow. Establishing a validated operating envelope therefore requires measured source conditions, overlapping A04 diagnostics with quantified detection limits and calibration uncertainties, and reconstruction of the incident distribution at the sample.

6.3. Two-Level Validation Protocol

The proposed validation sequence avoids tuning the surface model to compensate for an incorrectly known facility flow:

1) *Facility-flow calibration and validation.* Source and background parameters are calibrated against a defined subset of A04 measurements. The resulting facility DSMC solution is then assessed against held-out spatial or diagnostic data. Its output is the incident distribution at the sample with an uncertainty description.
2) *GSI-response validation.* For a documented material and surface state, the A01/A02 kernel predicts an observable that was not used in facility calibration. Simulation and experiment are compared using the combined numerical, model-form, and measurement uncertainty.

The first end-to-end demonstrator should use alumina because the A01 scattering database and A02 cVAE transfer already overlap for this material. The surface preparation must be documented sufficiently to assign an A01 surface-state class. The incident state should lie inside the trained kernel domain, and the comparison metric should be agreed before the experimental data are examined.

7. DISCUSSION

The workflow replaces an implicit sequence of project outputs by explicit probabilistic interfaces. This change exposes four ways in which the chain can fail.

First, the atomistic database may omit a state variable that is important at the mesoscopic scale. Oxygen coverage is the most immediate example: it is produced by previous impacts and changes both scattering and chemistry. A stationary kernel is justified only if the surface state is stationary over the relevant exposure or is represented explicitly.

Second, a generative kernel may reproduce the marginal reflected-velocity distribution while violating joint correlations or conservation properties that determine force. Validation must therefore include force-relevant moments and conditional distributions, not only visual agreement of histograms.

Third, uncertainty may be reduced at one scale but reintroduced at the next. MFMC reduces sampling error for selected macroscopic moments; it does not remove wall-model discrepancy, atmospheric model uncertainty, or experimental calibration error. An end-to-end uncertainty budget should distinguish parameter uncertainty, finite-sample uncertainty, surrogate error, model discrepancy, and measurement error.

Fourth, the facility and orbit represent different domains. The ground facility is valuable because it provides controlled, repeatable conditions, but its composition, velocity distribution, background gas, and sample history will not reproduce all on-orbit states simultaneously. The objective of facility validation is therefore not to certify the entire VLEO envelope in one experiment. It is to test

CC BY 4.0

TAB 2. Proposed validation matrix. The final observable in the third row must be selected according to the attainable signal and diagnostic access.

Level	Simulation quantity	Experimental information	Principal uncertainties
Facility field	$n(\boldsymbol{x})$, $\boldsymbol{u}(\boldsymbol{x})$, flux, composition, energy distribution	Probe scans, mass spectrometry, FIPEX, optical or time-of-flight data	Source inflow, background pressure, skimmer geometry, diagnostic calibration and spatial resolution
Sample boundary	Incident distribution $f_i(\boldsymbol{v}, s)$ at the material location	Reconstructed local state from overlapping diagnostics	Interpolation to the sample, temporal stability, species-dependent transmission
Surface response	Reflected distribution, adsorption/product yield, momentum or energy transfer	Independent GSI-response observable and acceptance metric not yet selected	Surface roughness/coverage, kernel extrapolation, finite signal, facility-to-orbit domain shift
Macroscopic propagation	C_D, C_L, force and moment distributions	Future force balance, flight data, or propagation of validated component models	Geometry, attitude, atmosphere, model discrepancy and identifiability

individual interfaces under well-characterized conditions and to establish where extrapolation begins.

At the current maturity, three links are demonstrated: atomistic scattering trends for alumina, generative transfer of selected reflected distributions to a DSMC wall boundary, and cost-efficient propagation of environmental uncertainty to drag moments. The facility reconstruction and diagnostic chain are in progress, and the complete surface-response validation is planned. This status distinction should be preserved in future reporting.

8. CONCLUSIONS AND NEXT STEPS

This paper presented an atomistic-to-macroscopic workflow for AO gas–surface interactions in VLEO and organized the activities of ATLAS projects A01–A04 around their transferred quantities. A01 provides state-dependent atomistic outcome statistics. A02 converts reflected-velocity data into a conditional generative wall kernel, embeds it in DSMC, and propagates the response to aerodynamic coefficients and uncertainty estimates. A03 and A04 provide the complementary facility reconstruction and diagnostic measurements required to define a traceable experimental boundary condition.

The principal scientific result of the synthesis is that the scale interfaces must retain more information than an accommodation coefficient: incident state, surface state, correlated outgoing state, event class, and uncertainty. The numerical A01–A02 chain is demonstrated for selected alumina scattering cases, whereas reactive surface evolution and the full experimental loop remain incomplete.

The next milestone is one pre-defined end-to-end alumina demonstrator. It requires (i) a documented surface class shared by atomistic simulation and experiment, (ii) a facility condition inside the numerical kernel domain, (iii) calibration and held-out validation of the local incident flow, and (iv) an independent surface-response observable with a pre-defined acceptance criterion. Completing this demonstrator will turn the current set of compatible methods into a quantitatively testable predictive chain.

ACKNOWLEDGMENT

This work is funded by the Deutsche Forschungsgemeinschaft (DFG, German Research Foundation), Project-ID 516238647, CRC 1667 ATLAS. The authors acknowledge the contributions of all members of the ATLAS project area A and the computing resources used for the atomistic and rarefied-flow simulations.

Contact address:

jovan.boskovic@iag.uni-stuttgart.de

References

[1] S. Hocker, H. Lipp, N. Segreto, J. Roth, and J. Kästner. Impact of hyperthermal oxygen on alumina surfaces investigated by molecular dynamics simulations. *CEAS Space Journal*, 18:575–587, 2026. DOI: 10.1007/s12567-025-00656-1.

[2] M. Schütte, S. Hocker, H. Lipp, J. Roth, S. Fasoulas, and M. Pfeiffer. A machine learning framework for scattering kernel derivation using molecular dynamics data in very low Earth orbit. *Physics of Fluids*, 37(9), 2025. DOI: 10.1063/5.0287359.

[3] J. Boskovic, M. Pfeiffer, and A. Beck. Moment-specific multifidelity Monte Carlo for efficient estimation of VLEO drag statistics: A benchmark study, 2026.

[4] M. Schütte, S. Hocker, H. Lipp, J. Roth, S. Fasoulas, and M. Pfeiffer. Conditional normalizing flow for gas-surface scattering from ther-

CC BY 4.0

mal to hypersonic velocities. *arXiv*, 2026. DOI: 10.48550/arXiv.2606.31928.

[5] The PICLas Developers. PICLas: A 3D particle-based kinetic simulation framework combining PIC, DSMC, BGK, and Fokker-Planck methods for plasma dynamics and rarefied gas flows. https://github.com/piclas-framework/piclas, 2016.

[6] L. A. Sinpetru, N. H. Crisp, D. Mostaza-Prieto, S. Livadiotti, and P. C. E. Roberts. ADBSat: Methodology of a novel panel method tool for aerodynamic analysis of satellites. *Computer Physics Communications*, 275, 2022. DOI: 10.1016/j.cpc.2022.108326.

[7] F. Turco, C. Traub, M. Schütte, M. Pfeiffer, and S. Fasoulas. Assessment of the practicality of optimal aerodynamic orbit control in VLEO. *Acta Astronautica*, 245, 2026. DOI: 10.1016/j.actaastro.2026.02.039.

[8] G. A. Bird. *Molecular Gas Dynamics and the Direct Simulation of Gas Flows*. Clarendon Press, Oxford, U.K., 1994.

[9] S. Fasoulas, C.-D. Munz, M. Pfeiffer, J. Beyer, T. Binder, S. Copplestone, S. Mirza, and P. Nizenkov. Combining particle-in-cell and direct simulation Monte Carlo for the simulation of reactive plasma flows. *Physics of Fluids*, 31(7), 2019. DOI: 10.1063/1.5097638.

[10] A. Schlitzer, K. S. Ellenberger, C. Traub, S. Fasoulas, and G. Herdrich. Overview of ground-based facilities for atomic oxygen material testing. *Journal of Evolving Space Activities*, 4(626), 2026. DOI: 10.57350/jesa.262.

[11] Kim-Sophie Ellenberger, Alexander Schlitzer, Marcel Pfeiffer, and Stefanos Fasoulas. Numerical study on the setup of an atomic oxygen ground testing facility. In *3rd International Conference on Flight Vehicles, Aerothermodynamics and Re-entry (FAR), Arcachon, France*, 2025.

[12] M. Eberhart, S. Löhle, B. Strelnikov, J. Hedin, M. Khaplanov, S. Fasoulas, J. Gumbel, F.-J. Lübken, and M. Rapp. Atomic oxygen number densities in the mesosphere–lower thermosphere region measured by solid electrolyte sensors on WADIS-2. *Atmospheric Measurement Techniques*, 12:2445–2461, 2019. DOI: 10.5194/amt-12-2445-2019.

[13] S. Löhle. *Untersuchung von Wiedereintrittsplasmen mit Hilfe laserinduzierter Fluoreszenzmessungen*. PhD thesis, Institut für Raumfahrtsysteme, Universität Stuttgart, Stuttgart, Germany, 2006.

[14] P. Bogen, Ph. Mertens, E. Pasch, and H. F. Döbele. Detection of atomic oxygen and hydrogen in the vacuum UV using a frequency-doubled, Raman-shifted dye laser. *Journal of the Optical Society of America B*, 9(12):2137–2141, 1992. DOI: 10.1364/JOSAB.9.002137.

[15] J. R. Wubs. *Terahertz Absorption Spectroscopy for Measuring Atomic Oxygen Densities: Development and Comparison with Established Techniques*. PhD thesis, Mathematisch-Naturwissenschaftliche Fakultät, Universität Greifswald, Greifswald, Germany, 2024.

CC BY 4.0